Photoconductivity induced by nanoparticle segregated grain-boundary in spark plasma sintered BiFeO₃

Subhajit Nandy, Pavana S. V. Mocherla, and C. Sudakar

Photoconductivity induced by nanoparticle segregated grain-boundary in spark plasma sintered BiFeO₃

Subhajit Nandy, Pavana S. V. Mocherla, and C. Sudakar[a)]
Multifunctional Materials Laboratory, Department of Physics, Indian Institute of Technology Madras, Chennai 600036, India

Photoconductivity studies on spark plasma sintered BiFeO₃ samples with two contrasting morphologies, viz., nanoparticle-segregated grain boundary (BFO-AP) and clean grain boundary (BFO-AA), show that their photo-response is largely influenced by the grain boundary defects. Impedance analyses at 300 K and 573 K clearly demarcate the contributions from grain, grain-boundary, and the nanoparticle-segregated grain-boundary conductivities. I-V characteristics under 1 sun illumination show one order of higher conductivity for BFO-AP, whereas conductivity decreases for BFO-AA sample. Larger photocurrent in BFO-AP is attributed to the extra conduction path provided by oxygen vacancies on the nanoparticle surfaces residing at the grain boundaries. Creation of photo-induced traps under illumination and the absence of surface conduction channels in BFO-AA are surmised to result in a decreased conductivity on illumination. *Published by AIP Publishing.* [http://dx.doi.org/10.1063/1.4983764]

I. INTRODUCTION

BiFeO₃ (BFO) is a unique multiferroic material in which coupling between ferroic order parameters was exploited to control the magnetization and polarization using electric and magnetic fields, respectively.[1] In recent years, this material has also been explored for photovoltaic (PV) and photoferroelectric (PFE) applications.[2–6] The prominent merits of using ferroelectric oxides in photovoltaic applications include the inherent separation between positive and negative charges due to the domain walls unlike in case of pn-junctions where charge carriers are separated by the electric field developed at the depletion region; high structural and chemical stabilities; and their benign impact on the environment.[4,5] Another significant attribute of using ferroelectric oxides is the possibility of obtaining photovoltages much larger than bandgap contrary to semiconducting oxides wherein the carrier generation and corresponding photovoltage are limited to the bandgap of the material.[7] However, a major hindrance in the progress of photovoltaic studies using ferroelectrics is their insulating nature with bandgap ∼3 eV.[4] This large bandgap renders the photoabsorption low, thereby affecting the overall device performance. Hence, ferroelectric oxide materials with narrow bandgap are of immense need in producing highly efficient, chemically stable solar cell devices.

BiFeO₃ has captured a great deal of attention for the reason that it is the only ferroelectric material with a relatively small bandgap value ∼2.5 eV in bulk form.[8] By controlling the size and microstrain, bandgap tunability from 2.32 eV to 2.1 eV has been shown in pure BiFeO₃ nanoparticles.[9] Ca doping at Bi³⁺ site has resulted in a systematic reduction in the bandgap of BiFeO₃ from 2.3 eV to 1.5 eV via oxygen vacancy-induced structural modulations.[10] Several reports have shown drastic difference in the bandgap values of

BiFeO₃ by altering their size,[9] stress/strain,[11] composition,[12,13] and morphology,[14] further confirming the viability of bandgap tuning in BiFeO₃, which is an essential attribute to achieve high efficiency in photovoltaic devices. A way to check the photosensitivity of BiFeO₃ is to test the photocurrent or photovoltage characteristics. Photocurrent responses and switchable photovoltaic effect in BiFeO₃ have been shown for many configurations,[2,6,15–23] and photoconductivity in bulk BiFeO₃[3,15,24,25] has also been reported widely. Photovoltages of more than 15 V were observed in BiFeO₃ thin films by modulating the domain wall arrangement.[7] Alexe *et al.* have shown mapping of the generation and recombination of charge carriers in BiFeO₃ using photoinduced transient spectroscopy in combination with scanning probe microscopy.[26] From this study, it is proposed that domain walls contribute very minimal to the photovoltaic phenomenon and that the photoresponse and carrier life time largely depend on the defect states present in the material.[26] By contrast, Bhatnagar *et al.*[27] have shown that by controlling the conductivity of domain walls, large open circuit voltages (V_OC) ∼50 V can be obtained and that the domain walls are more conductive than the bulk. Photocarriers can be efficiently collected with an improvement in the photoconversion efficiency by seven orders of magnitude as demonstrated using a nanoscale top electrode.[28] Hung *et al.*[25] observed that the photovoltage and photocurrent density of BiFeO₃ exhibit non-linear dependence on illuminated light intensity. Oxygen vacancies in Ca doped BiFeO₃ were shown to produce dark conductivity 10 times higher than that in pure BiFeO₃.[29] A switchable diode-like effect in BiFeO₃ single crystals is demonstrated by Choi *et al.*,[30] and the photovoltaic response is said to have an influence from migration of defects such as oxygen vacancies. A persistent photoconductivity in strained BiFeO₃ thin films related to the charged trap levels under illumination and subsequent thermal emptying is demonstrated by Bhatnagar *et al.*[31]

[a)]Author to whom correspondence should be addressed: csudakar@iitm.ac.in. Telephone: +91-44-22574895.

In spite of significant research, the influence of microstructure and defects on the photoresponse of $BiFeO_3$ remains to be addressed.

In this report, we show that the nature of grain boundary plays a significant role in controlling the photoconduction of spark plasma sintered (SPS) $BiFeO_3$ samples. We compare the photoresponses of two samples with marked morphological differences, one with nanoparticle-segregated grain boundary (BFO-AP) and the other with clean grain boundary (BFO-AA). The defects, particularly, oxygen vacancies on the nanoparticle surfaces located at the grain boundaries in BFO-AP, provide conductive paths and are responsible for transport of charge carriers across the grains, thus enhancing the photoconductivity in bulk $BiFeO_3$. By contrast, modification of boundary structures in BFO-AA resulted in poor photoconduction. Interestingly, this sample shows an increase in resistivity under illumination. This reverse trend is attributed to the photo-induced trap level formed on illumination in addition to the absence of conductive channels.

II. EXPERIMENTAL

$BiFeO_3$ nanoparticles were prepared by a low temperature citrate sol-gel process.[9] The precursor powder was calcined at 550 °C for 1 h in air to obtain nanocrystalline $BiFeO_3$ phase with a particle size of ∼50 nm. The powder was then pressed into dense (99.9%) pellets using SPS technique, in which a graphitic die of 20 mm diameter loaded with $BiFeO_3$ powder was subjected to uniaxial pressure of 40 MPa at 650 °C for 5 min under vacuum. Sintering parameters such as pressure, temperature, and time were optimized in order to minimize rapid grain growth of $BiFeO_3$. The sintered pellets were polished to eliminate carbon from the surface of the pellets. The phase purity and crystallinity of $BiFeO_3$ pellets were analyzed using x-ray diffraction (XRD) patterns recorded on a X'Pert-Pro, Panalytical powder diffractometer using Cu-Kα radiation ($\lambda = 1.5406$ Å). The phase and structural details of $BiFeO_3$ were also studied using Raman spectroscopy with a 632 nm red excitation line of He–Ne laser using Horiba Jobin-Yvon (HR800 UV) micro-Raman spectrometer. Field emission scanning electron microscopy (FESEM) was carried out using a Quanta 400, FEI microscope. Microstructural details were analyzed from transmission electron microscope images (TEM) obtained using a FEI (TECNAI G2 T20) operating with an applied voltage of 200 kV. Impedance spectroscopy of BFO samples were studied at 30 °C and 300 °C using a dielectric resonance spectrometer (Novocontrol Technologies). The pellets were silvered on either sides, and impedance variation was recorded in the frequency range of 100 Hz to 40 MHz. Photoconductivity measurements on the BFO pellets were carried out at room temperature (300 to 305 K) using the van der Pauw four-probe method. Silver point contacts on the pellets were connected with thin copper wires. The point contacts were made on the periphery of the pellets of area ∼0.25 cm^2 and thickness ∼1 mm. I-V characteristics and voltage change at a constant current under dark and AM 1.5 one sun illumination (100 mW/cm^2) were measured using Keithley 2400 source meter.

III. RESULTS AND DISCUSSION

FESEM images of the as-prepared $BiFeO_3$ SPS pellet (referred to as BFO-AP) showed large grains of size ranging from 1 μm to 2 μm [Fig. 1(a)]. The image also shows the presence of nanoparticles in the size range of 100–200 nm along the grain boundaries. It should be noted that the nanoparticle size at the grain boundary is found to be larger than the average size of $BiFeO_3$ nanoparticles (∼50 nm) taken in
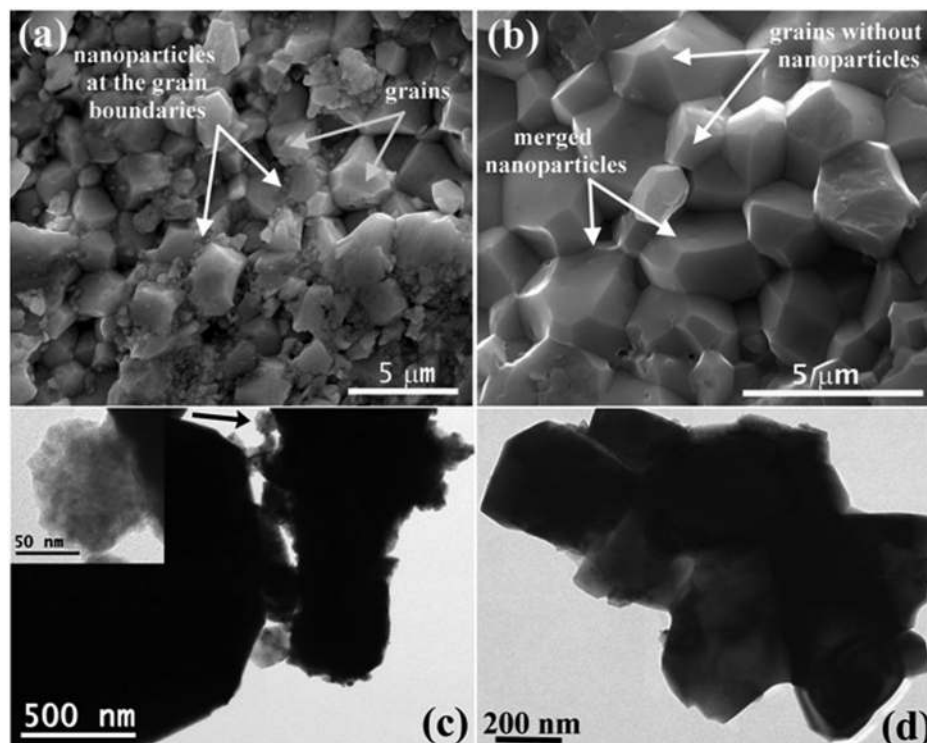

FIG. 1. FESEM images of (a) BFO-AP sample where the grain growth is incomplete with nanoparticles located at the grain boundaries (white arrows). (b) BFO-AA sample where uniform grain formation with sharp grain boundaries is observed. Bright field TEM images of (c) BFO-AP and (d) BFO-AA samples. The grain boundaries in BFO-AP are found to be filled with nanoparticles. The inset shows one such nanoparticle which is an agglomerate of much smaller particles. BFO-AA shows clean grain boundaries without nanoparticles.

the powder sample. This clearly indicates that the micron sized grains in the SPS pellets have grown at the expense of smaller nanocrystallites during the sintering process. However, the short sintering time (5 min) led to an incomplete grain growth, especially at the grain boundaries where nanoparticles were found to coexist. BFO-AP pellets were further annealed at 550 °C for 15 min in air (referred to as BFO-AA). The process removes nanoparticles from the grain boundaries by allowing a complete grain growth and annihilates the oxygen vacancies present at the grain boundaries. FESEM images of BFO-AA depict a clear difference in the morphology change at the grain boundaries [Fig. 1(b)]. The nanoparticles have grown and merged with neighbouring large grains, leaving the boundaries clean. The same has also been confirmed from the bright field transmission electron microscopy (TEM) images [Figs. 1(c) and 1(d)]. In BFO-AP, it was observed that some of the nanoparticles at the grain boundaries are in fact agglomerates of smaller nanoparticles of few ten nanometers [Fig. 1(c)]. Nevertheless, the average size of large grains has not changed considerably, ensuring a homogeneous morphology after air-annealing.

The x-ray diffraction (XRD) of BFO-AP and BFO-AA SPS pellets [Fig. 2(a)] shows $BiFeO_3$ as the major phase in both samples. A small percentage of $Bi_2Fe_4O_9$ is found as a secondary phase which is discernible in sintered pellets [Fig. 2(a)]. It is well-known that any slight deviation from the
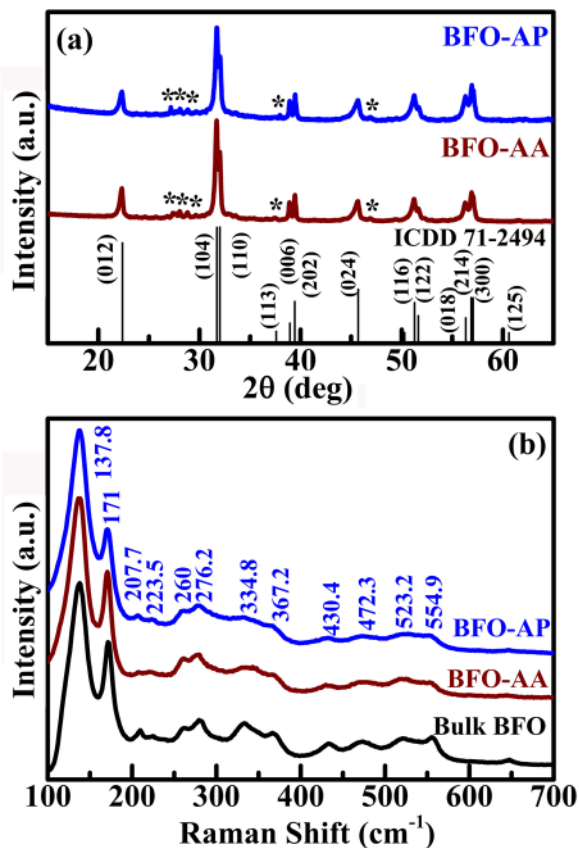

FIG. 2. (a) XRD patterns of as-prepared (BFO-AP) and air-annealed (BFO-AA) $BiFeO_3$ SPS pellets. "*" indicates the presence of trace quantities of $Bi_2Fe_4O_9$. (b) Raman spectra of BFO-AP and BFO-AA SPS pellets. Both the spectra show all the modes pertaining to the rhombohedral crystal structure as compared with the spectrum of bulk $BiFeO_3$.

thermodynamic conditions can lead to the segregation of small percentage of secondary phases like $Bi_2Fe_4O_9$.[32] This is seen more prominently when the samples are annealed at high temperatures (>650 °C) or like in our case when the samples are spark plasma sintered.[33,34] This secondary phase does not affect the photoconductivity in the samples since both the AP and AA samples have this phase and show different photoconductivity behaviors. All the peaks in the diffraction patterns were indexed with respect to the standard ICDD file #71-2494 of $BiFeO_3$ with a rhombohedral structure ($R3c$ space group). Raman spectra on BFO-AP and BFO-AA samples were collected with 632 nm excitation from He-Ne laser [Fig. 2(b)]. $BiFeO_3$ with a distorted perovskite structure with space group $R3c$ shows a total of 13 ($4A_1 + 9E$) Raman active modes.[35] Apart from first two strong E(TO) modes at 140 and 174 cm^{-1}, the other modes are observed at 212, 227, 263, 282, 335, 371, 435, 476, 524, 558, and 650 cm^{-1}, corresponding to pure $BiFeO_3$ phase. All these values match very close with the data reported by Palai et al.[35] Both the samples show the spectra corresponding to the rhombohedral structure without any modes from secondary phase.

We carried out impedance spectroscopy analysis on both BFO-AP and BFO-AA samples to understand the difference in their electrical properties with respect to the microstructural features. The pellets were silvered on either sides, and frequency dependent (100 Hz to 40 MHz) impedance variation was studied at 30 °C and 300 °C using a dielectric resonance spectrometer (Novocontrol Technologies). Figure 3 shows the Nyquist plots (Z′ vs. Z″) of BFO-AP and BFO-AA measured at 30 °C and 300 °C. These plots are fitted using Z-view program with model RC circuits connected in series (insets of Fig. 3), and the fitted parameters are given in Table I. Nyquist plots reveal that for the room temperature measurements, there exist two semicircles for BFO-AP and one semicircle for BFO-AA. The diameter of the semicircle towards high frequency denotes the grain resistance and that towards the low frequency denotes grain boundary resistance. The electrode polarization can be neglected as it dominates only at very low frequencies. BFO-AA showed only grain resistance (2.5×10^7 Ω), which is two orders of magnitude larger than that of BFO-AP (1.3×10^5 Ω). The grain resistance in both these samples is found to be lower than the reported resistivity of BFO single crystal (6×10^{10} Ω cm).[24,36] Even in bulk ceramics, the resistivity is shown to be in the range of 10^7 Ω cm. Oxygen annealing has shown to result in an increase in the resistivity,[33] which is consistent with an increase observed in our samples after air annealing. We attribute this change in the grain resistance to the annihilation of oxygen vacancies in BFO-AA on air annealing. Grain boundary conductivity of BFO-AA is found to be negligible. These impedance plots clearly show that the increase in resistance of BFO-AA is due to merging of nanoparticles with larger grains after annealing. To resolve the mechanism of conduction, we carried out measurement on the same samples at 300 °C. At this temperature, BFO-AP shows three discernible semicircles, and BFO-AA shows two semicircles. The data are fitted with corresponding equivalent circuits as shown in the insets of Figs. 3(c) and 3(d). The extra semicircle seen for BFO-AP at 300 °C clearly demarcates the
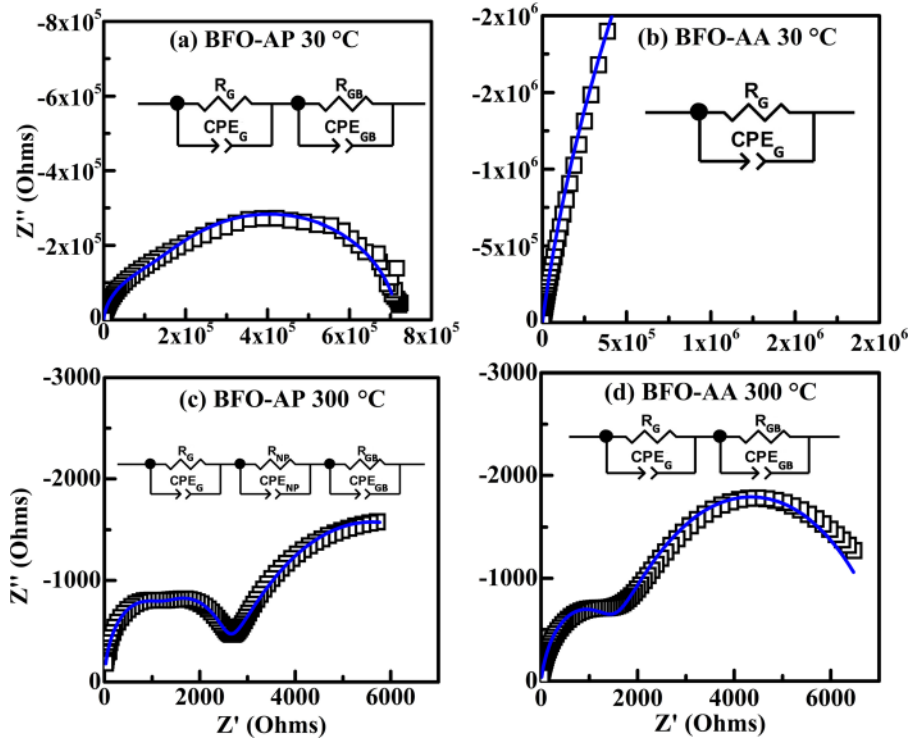
FIG. 3. Room temperature Nyquist plots of (a) BFO-AP and (b) BFO-AA samples. (c) and (d) The Nyquist plots for the same samples at 300 °C. The circuits used for fitting the impedance curves are shown as insets in the respective plots. Open symbols are the measured data, and the solid line is the fitted curve.

contribution from nanoparticles residing at the grain boundaries apart from the actual grain boundary contribution. It should be noted that the measurement temperature (300 °C) is far below the crystallization ($\sim$400 °C) and grain growth ($>$500 °C) temperatures in $BiFeO_3$. Therefore, we are sure that the microstructure remains same during the high temperature (300 °C) impedance studies. The effect of air annealing on the BFO-AP pellet, where nanoparticles present at the grain boundary disappear, is clearly reflected in the Nyquist plot. BFO-AA shows two semicircles corresponding to grain and grain boundary contributions. Thus, it is clear that the BFO-AP samples have three sources of impedance mainly arising from (i) grain, (ii) nanoparticles present at grain boundary, and (iii) the grain boundary itself. On the other hand, impedance of BFO-AA is only due to the grain and grain boundary contributions. The increase in the grain resistance by two orders in annealed sample also suggests a significant suppression of boundary related vacancy contribution.

Photoconductivity measurements on the BFO-AP and BFO-AA pellets were carried out by the van der Pauw four-probe method. I-V characteristics and voltage change at a constant current under dark and AM 1.5 one sun illumination (100 mW/cm^2) measured using Keithley 2400 source meter are shown in Fig. 4. I-V characteristics of BFO-AP [Fig. 4(a)]

and BFO-AA [Fig. 4(b)] pellets under both dark and light illumination show significant difference in the electrical properties. BFO-AP shows two orders higher conduction current than BFO-AA. Interestingly, BFO-AP sample shows one order increase in current under 1 sun illumination at a low voltage; however, BFO-AA shows an order decrease in the current even at high voltages. The low current density in BFO-AA compared to BFO-AP corroborates well with its large resistance observed from impedance studies.

The voltage is monitored as a function of time at constant current with light ON and OFF for several cycles. The voltage change under constant current is plotted as conductivity vs. time for three cycles [Figs. 4(c) and 4(d)]. The conductivity of BFO-AP pellet is found to increase by an order when the light is turned ON [Fig. 4(c)]. This change is not spontaneous, we find that the conductivity saturates in $\sim$5 min. When the light is turned OFF, the conductivity decreases slowly back to the original value. Interestingly for BFO-AA, we find a reverse trend in the conductivity change, i.e., the conductivity decreases by 4 times on exposing the materials to light [Fig. 4(d)]. It returns to the original state on turning OFF the light. The conductivity change in both the BFO-AP and BFO-AA samples with the exposure of light clearly suggests a significant photoresponse in $BiFeO_3$.

TABLE I. Micron sized grain resistance (R_G), resistance from nanoparticles at the boundaries (R_{NP}), grain boundary resistance (R_{GB}), and corresponding capacitances C_G, C_{NP}, and C_{GB} are listed. All these values for BFO-AP and BFO-AA are given for measurements done at 30 °C and 300 °C.

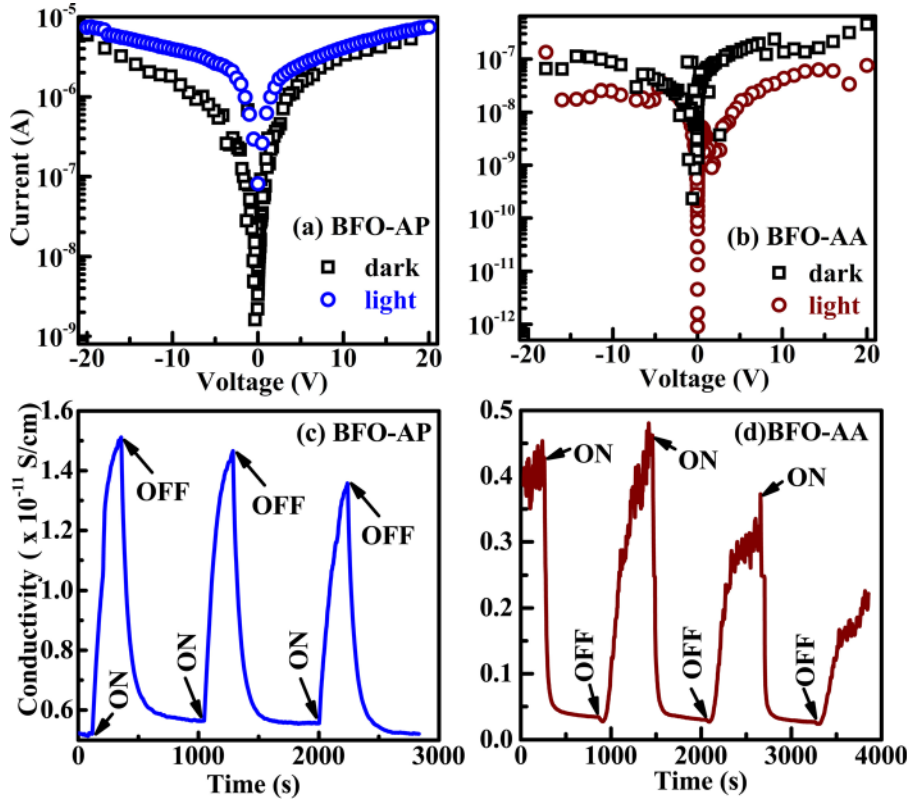| Sample	T (°C)	R_G (Ω)	C_G (F)	R_{NP} (Ω)	C_{NP} (F)	R_{GB} (Ω)	C_{GB} (F)
BFO-AP	30	1.28×10^5	9.87×10^{-11}	...	...	5.89×10^5	2.13×10^{-10}
BFO-AA	30	2.49×10^7	2.71×10^{-10}	...	...	...	...
BFO-AP	300	1120	2.88×10^{-11}	1336	5.81×10^{-10}	6315	1.22×10^{-6}
BFO-AA	300	1389	1.7×10^{-9}	...	...	5977	2.31×10^{-7}

FIG. 4. I-V characteristics of (a) BFO-AP and (b) BFO-AA SPS pellets under the ON (light-open circles) and OFF (dark-open squares) conditions of the solar simulator. Photoconductivity response of (c) BFO-AP and (d) BFO-AA SPS pellets under the ON and OFF states of AM 1.5 source.

We estimated the average carrier generation lifetime (τ_g) for the rising part of the conductivity in BFO-AP using the equation $\frac{\sigma_t - \sigma_{off}}{\sigma_{on} - \sigma_{off}} = \frac{\Delta\sigma_t}{\Delta\sigma_{total}} = a\left(1 - e^{-\frac{t}{\tau_g}}\right)$, where $\Delta\sigma_t$ ($= \sigma_t - \sigma_{off}$) is the difference in conductivity at any time (σ_t) with respect to OFF condition (σ_{off}), $\Delta\sigma_{total}$ ($= \sigma_{on} - \sigma_{off}$) is the

difference in the conductivity between the ON (σ_{on}) and OFF (σ_{off}) states, and a is a constant. The decreasing part of the conductivity is fitted with a stretched exponential function $\frac{\sigma_t - \sigma_{off}}{\sigma_{on} - \sigma_{off}} = \frac{\Delta\sigma_t}{\Delta\sigma_{total}} = a\, e^{-\left(\frac{t}{\tau_r}\right)^b}$, where τ_r is carrier recombination life time, a is a constant, and b indicates the deviation
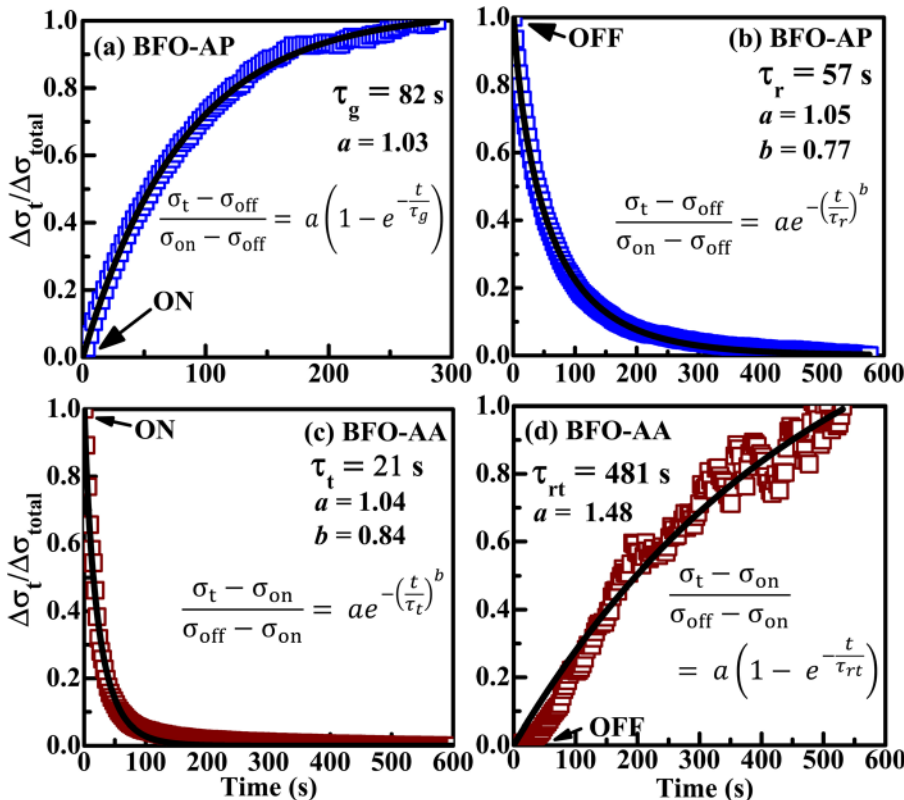

FIG. 5. (a) The increasing segment during the light ON and (b) the decreasing segment during the light OFF conditions of photoconductivity response for BFO-AP. (c) The decreasing segment during light ON and (d) the increasing segment during the light OFF conditions of photoconductivity response of BFO-AA. The open symbols show the measured response; solid line is the exponential fit.

from exponential function. We find that τ_g is $\sim$82 s and τ_r $\sim$57 s for BFO-AP. Since the photoconductivity in BFO-AA exhibits a reverse trend, we used the stretched exponential function $\frac{\sigma_t - \sigma_{on}}{\sigma_{off} - \sigma_{on}} = \frac{\Delta\sigma_t}{\Delta\sigma_{total}} = a\, e^{-\left(\frac{t}{\tau_t}\right)^b}$ for the decreasing segment in ON state. Here, τ_t corresponds to the photoinduced trap generation lifetime, which is found to be $\sim$21 s for BFO-AA. Despite a large number of photoconductivity studies on bulk $BiFeO_3$ ceramic samples, there are no reports which estimated photoinduced trap generation lifetime. It is known that in semiconductors, the recombination rate slows down due to trap states between valance band and conduction band. The presence of carrier trapping can have a strong effect on the measured response time, causing it to be much longer than the actual lifetime.[37] When the light is turned OFF, the conductivity returns to its initial value due to the release of trapped charge carriers. The equation $\frac{\sigma_t - \sigma_{on}}{\sigma_{off} - \sigma_{on}} = \frac{\Delta\sigma_t}{\Delta\sigma_{total}} = a\left(1 - e^{-\frac{t}{\tau_{rt}}}\right)$, where a is a constant and τ_{rt} is the trapped charge carrier recovery time constant used to fit the data (Fig. 5). We find that τ_{rt} is $\sim$481 s, indicating that the release of trapped carriers in OFF state is not

spontaneous and takes place for a longer time. Such persistent photo-resistive nature arises as the traps are active and carriers remain trapped for a longer time. Wavelength dependent photoconductivity measurements were also carried out using UV LED ($\lambda = 395$ nm), green light ($\lambda = 550$ nm), and red light ($\lambda = 650$ nm) in the same four probe configuration (Fig. 6). The BFO-AP sample showed higher photoconductivity than BFO-AA in all the cases. The magnitude of photocurrent, however, seems to decrease with the increase in wavelength for both the samples. BFO-AA shows a reverse conduction for UV similar to that observed with AM1.5. We could see some measurable photoconductivity response in the BFO-AP sample with green light, but BFO-AA shows a very poor response to the green light. For red source, both BFO-AP and BFO-AA show no response. High resistive nature and poor response at high wavelengths make the photoresponse in BFO-AA fall close to the noise levels. The ON and OFF segments of the photoconductivity curves for BFO-AP and BFO-AA using UV source were fitted in the same way as for AM1.5 light (Fig. 7).
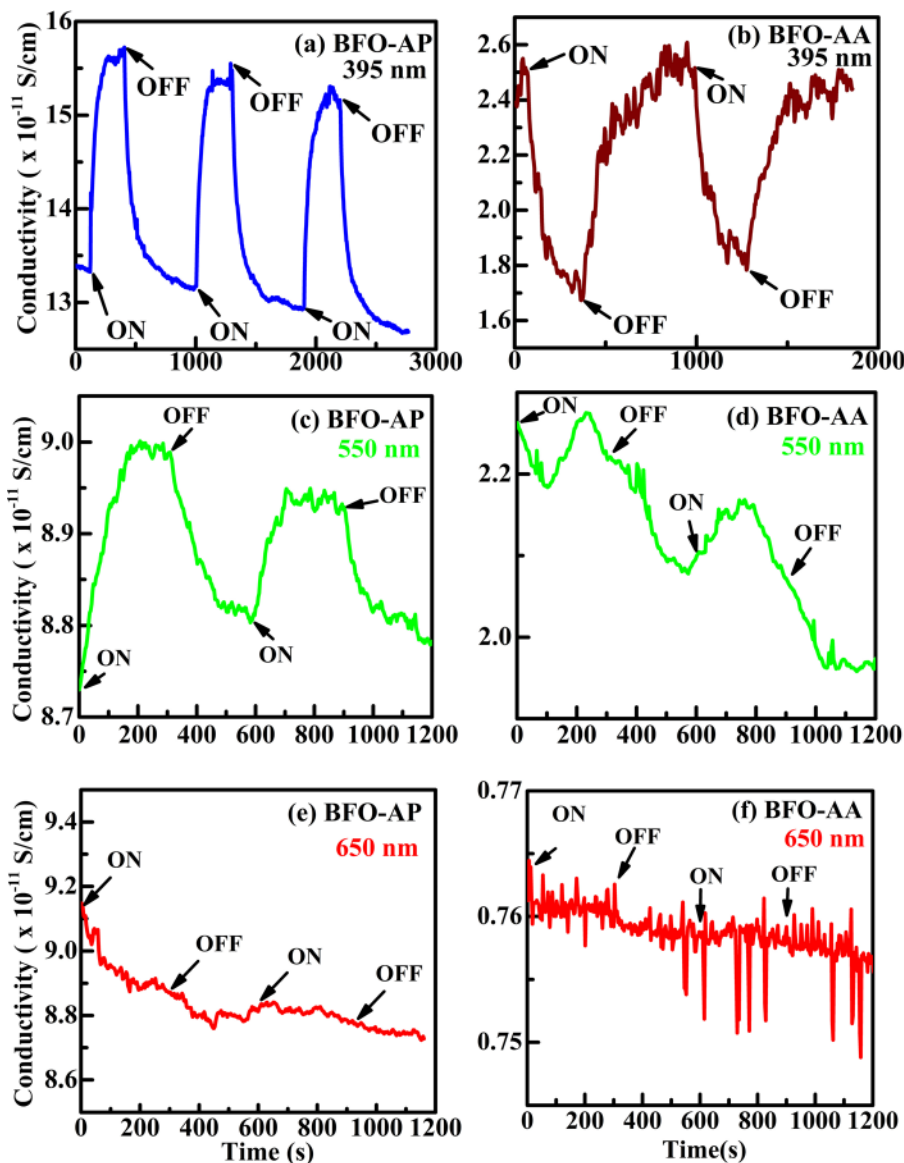

FIG. 6. Photoconductivity response of BFO-AP sample under (a) UV LED (395 nm), (c) green light (550 nm), and (e) red light (650 nm) illumination. The responses of BFO-AA sample under UV LED, green, and red illumination are shown in (b), (d), and (f), respectively.
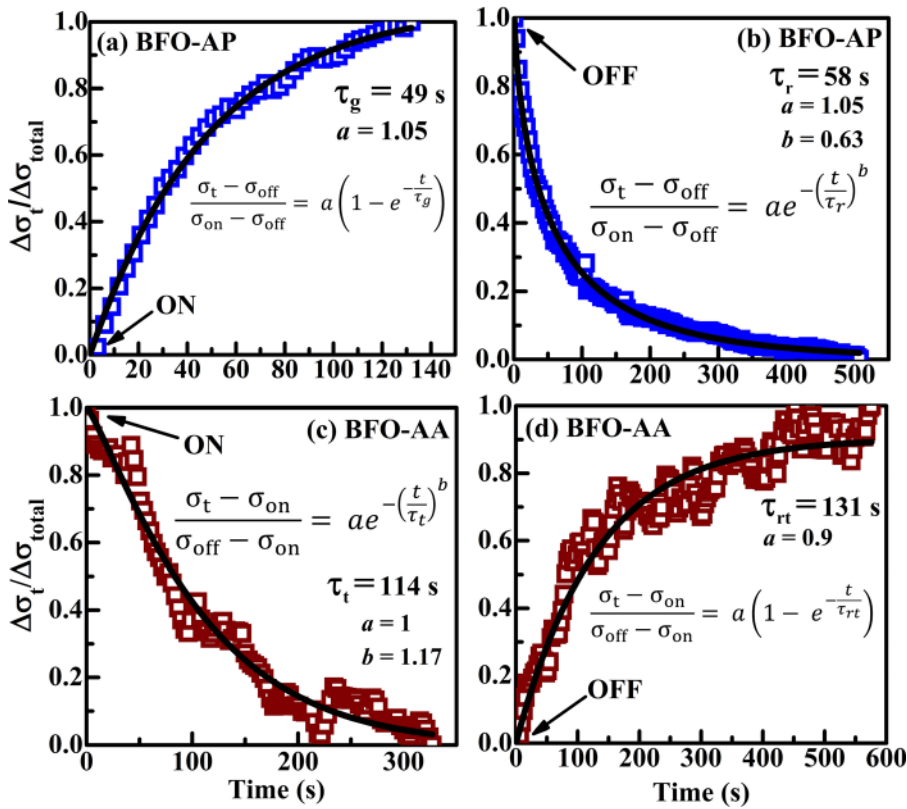
FIG. 7. The increasing and decreasing segments of the photoconductivity in the BFO-AP and BFO-AA samples under UV LED (395 nm) are fitted with exponential function as shown in (a), (b) and (c), (d), respectively.

In an ideal semiconductor, photocurrent is generated by the injection of electrons from the valence band to the conduction band under irradiation, and generation/recombination lifetimes of the charge carriers are same. Different lifetimes for the photocarriers imply that the photoconduction mechanism involves one or more energy levels in the bandgap.[26] In BFO-AP, the surfaces of nanoparticles present at the grain boundaries host large number of oxygen vacancies. Our previous studies on $BiFeO_3$ nanoparticles have shown that the surfaces are more disordered than the core. XPS studies have confirmed an increase in oxygen defects in smaller particles.[9,10] The shallow impurity levels created by these oxygen vacancies (denoted as NPSV in Fig. 8) provide additional conduction path for the photocarriers generated within the grains. On the other hand, BFO-AA with clean grain boundaries lacks such conduction channels and exhibits high resistance. Thus, the presence of nanoparticles at the grain boundary induces large photoconductivity in BFO-AP compared to BFO-AA. The reverse trend observed in the conductivity response for BFO-AA, i.e., a drop in conductivity on illumination, could be due to the predominant role of photo-induced traps.

Ionized oxygen vacancies within the grains are known to act as defect centers, trapping some of the photoinduced carriers.[38,39] The trap states are known to arise due to localized defects (vacancies or substitutions) or imperfections in the lattice. In $BiFeO_3$, the localized oxygen vacancies and bismuth vacancies are two possible sources of trap states. While such trap levels could be present in both BFO-AP and BFO-AA, the surface defect states at the boundaries dominate the conduction process in the former. Surface vacancies in BFO-AP create shallow donor impurity levels due to the

large concentration of surface defects as shown schematically in Fig. 8. These states are always in thermal equilibrium with the conduction band, since a small amount of energy is sufficient to re-excite the carriers falling into these
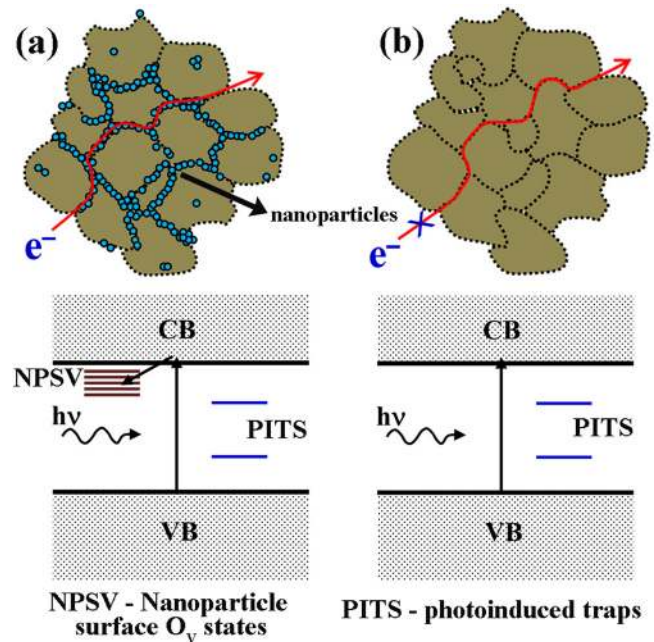

FIG. 8. Schematic for the morphologies of (a) BFO-AP and (b) BFO-AA in the SPS pellets. The corresponding band structures are given below. Deep levels (blue lines) symbolize photo-induced localized trap centers in the grain. The shallow states produced from surface oxygen vacancies from the nanoparticles at the grain boundaries (denoted as NPSV) in BFO-AP act like donor impurity levels, contributing to the easy conduction path for electrons (shown with red line in (a)).

states after emission from conduction band. In the absence of such states, as in the case of BFO-AA, the conductivity decreases and the electrons falling into deep traps stay for long time without being thermally activated/excited. These free electrons are more likely to capture a free hole before getting excited to conduction band.[40] The dominant role of traps in BFO-AA is substantiated by the longer recovery time ($\tau_{rt} \sim 481$ s) and quicker trap generation lifetime ($\tau_t \sim 21$ s) estimated from the photocurrent responses. The formation of these photoinduced traps is observed to be completely reversible, and after turning the illumination OFF, BFO-AA shows an increase in conductivity due to the release of trapped carriers back to their ground states.

IV. CONCLUSION

In conclusion, highly dense spark plasma sintered $BiFeO_3$ pellets with contrasting morphology, viz., (i) nanoparticle-segregated grain boundary (BFO-AP) and (ii) a clean grain boundary (BFO-AA), were studied for their electrical and photoresponse characteristics. BFO-AP shows an increase in conductivity under illumination, whereas the current drops in the case of BFO-AA. Surface oxygen vacancies of the nanoparticles located at the grain boundaries in BFO-AP provide additional conduction channels, resulting in larger photocurrent. Absence of surface conduction channels in BFO-AA leads to the dominance of photo-induced traps, resulting in a decreased conductivity on illumination. The effect of photo-induced trapping is observed to be completely reversible and the current resumes initial values in dark condition. These studies provide an insight and novel approach to tune the photo-response of $BiFeO_3$ via local microstructure modification at the grain boundaries.

[1]G. Catalan and J. F. Scott, Adv. Mater. **21**, 2463 (2009).
[2]T. Choi, S. Lee, Y. J. Choi, V. Kiryukhin, and S.-W. Cheong, Science **324**, 63 (2009).
[3]C. S. Tu, C. M. Hung, V. H. Schmidt, R. R. Chien, M. D. Jiang, and J. Anthoninappen, J. Phys.: Condens. Matter **24**, 495902 (2012).
[4]Z. Fan, K. Sun, and J. Wang, J. Mater. Chem. A **3**, 18809 (2015).
[5]K. T. Butler, J. M. Frost, and A. Walsh, Energy Environ. Sci. **8**, 838 (2015).
[6]S. Y. Yang, L. W. Martin, S. J. Byrnes, T. E. Conry, S. R. Basu, D. Paran, L. Reichertz, J. Ihlefeld, C. Adamo, A. Melville, Y.-H. Chu, C.-H. Yang, J. L. Musfeldt, D. G. Schlom, J. W. Ager, and R. Ramesh, Appl. Phys. Lett. **95**, 062909 (2009).
[7]S. Y. Yang, J. Seidel, S. J. Byrnes, P. Shafer, C. H. Yang, M. D. Rossell, P. Yu, Y. H. Chu, J. F. Scott, J. W. Ager, L. W. Martin, and R. Ramesh, Nat. Nano **5**, 143 (2010).
[8]B. Ramachandran, A. Dixit, R. Naik, G. Lawes, and M. S. R. Rao, Phys. Rev. B **82**, 012102 (2010).
[9]P. S. V. Mocherla, C. Karthik, R. Ubic, M. S. Ramachandra Rao, and C. Sudakar, Appl. Phys. Lett. **103**, 022910 (2013).
[10]S. V. M. Pavana, G. Sanjeev, C. Keun Hwa, M. S. R. Rao, and C. Sudakar, Mater. Res. Express **2**, 095012 (2015).
[11]H. Dong, Z. Wu, S. Wang, W. Duan, and J. Li, Appl. Phys. Lett. **102**, 072905 (2013).
[12]B. Ramachandran and M. S. Ramachandra Rao, J. Appl. Phys. **112**, 073516 (2012).
[13]X. S. Xu, J. F. Ihlefeld, J. H. Lee, O. K. Ezekoye, E. Vlahos, R. Ramesh, V. Gopalan, X. Q. Pan, D. G. Schlom, and J. L. Musfeldt, Appl. Phys. Lett. **96**, 192901 (2010).
[14]S. Li, Y.-H. Lin, B.-P. Zhang, Y. Wang, and C.-W. Nan, J. Phys. Chem. C **114**, 2903 (2010).
[15]C.-M. Hung, C.-S. Tu, W. D. Yen, L. S. Jou, M.-D. Jiang, and V. H. Schmidt, J. Appl. Phys. **111**, 07D912 (2012).
[16]R. L. Gao, Y. S. Chen, J. R. Sun, Y. G. Zhao, J. B. Li, and B. G. Shen, J. Appl. Phys. **113**, 183510 (2013).
[17]B. Liu, Z. Peng, J. Ma, J. Wang, Q. Zhao, and Y. Wang, Phys. Status Solidi A **210**, 819 (2013).
[18]H. W. Chang, F. T. Yuan, Y. C. Yu, P. C. Chen, C. R. Wang, C. S. Tu, and S. U. Jen, J. Alloys Compd. **574**, 402 (2013).
[19]Z. Peng, B. Liu, H. Zhu, Q. Zhao, and Y. Wang, Phys. Status Solidi A **209**, 1451 (2012).
[20]W. Dong, Y. Guo, B. Guo, H. Liu, H. Li, and H. Liu, Mater. Lett. **88**, 140 (2012).
[21]B.-C. Luo, C.-L. Chen, F. Fan, and K.-X. Jin, Chin. Phys. Lett. **29**, 018104 (2012).
[22]W. Le, J. Yu-ling, J. Kui-juan, W. Can, L. Hui-bin, W. Cong, G. Chen, C. Xi-yang, G. Er-jia, and Y. Guo-zhen, Europhys. Lett. **96**, 17008 (2011).
[23]W. Dong, Y. Guo, B. Guo, H. Li, H. Liu, and T. W. Joel, ACS Appl. Mater. Interfaces **5**, 6925 (2013).
[24]R. Moubah, O. Rousseau, D. Colson, A. Artemenko, M. Maglione, and M. Viret, Adv. Funct. Mater. **22**, 4814 (2012).
[25]C.-M. Hung, M.-D. Jiang, J. Anthoninappen, and C.-S. Tu, J. Appl. Phys. **113**, 17D905 (2013).
[26]M. Alexe, Nano Lett. **12**, 2193 (2012).
[27]A. Bhatnagar, A. Roy Chaudhuri, Y. Heon Kim, D. Hesse, and M. Alexe, Nat. Commun. **4**, 2835 (2013).
[28]M. Alexe and D. Hesse, Nat. Commun. **2**, 256 (2011).
[29]M. Kianinia, K. Ahadi, and A. Nemati, Mater. Lett. **65**, 3086 (2011).
[30]H. T. Yi, T. Choi, S. G. Choi, Y. S. Oh, and S. W. Cheong, Adv. Mater. **23**, 3403 (2011).
[31]A. Bhatnagar, Y. H. Kim, D. Hesse, and M. Alexe, Nano Lett. **14**, 5224 (2014).
[32]D. C. Arnold, K. S. Knight, G. Catalan, S. A. T. Redfern, J. F. Scott, P. Lightfoot, and F. D. Morrison, Adv. Funct. Mater. **20**, 2116 (2010).
[33]D. Zhonghua and A. Yukikuni, J. Phys. D.: Appl. Phys. **43**, 445403 (2010).
[34]R. Mazumder, D. Chakravarty, D. Bhattacharya, and A. Sen, Mater. Res. Bull. **44**, 555 (2009).
[35]R. Palai, H. Schmid, J. F. Scott, and R. S. Katiyar, Phys. Rev. B **81**, 064110 (2010).
[36]D. Lebeugle, D. Colson, A. Forget, and M. Viret, Appl. Phys. Lett. **91**, 022907 (2007).
[37]R. H. B. Alan and L. Fahrenbruch, *Fundamentals of Solar Cells: Photovolatic Solar Energy Conversion*, 1st ed. (Academic press, New York, 1983), Chap. 4, p. 90.
[38]Z. Peng and B. Liu, Eur. Phys. J. Appl. Phys. **71**, 30501 (2015).
[39]Y. Kenji, S. Wataru, M. Makoto, and Y. Toshinobu, Jpn. J. Appl. Phys., Part 1 **53**, 09PA17 (2014).
[40]A. Rose, Phys. Rev. **97**, 322 (1955).